Transient physics in the compression and mixing dynamics of two nanochannel-confined polymer chains

Lili Zeng,* Xavier Capaldi, Zezhou Liu, and Walter W. Reisner†
Department of Physics, McGill University, 3600 University Street, Montreal, Quebec H3A 2T8, Canada

(Received 27 November 2023; accepted 16 January 2024; published 20 February 2024)

We use molecular dynamics (MD) simulation and nanofluidic experiments to probe the non-equilibrium transient physics of two nanochannel-confined polymers driven against a permeable barrier in a flow field. For chains with a persistence length P smaller than the channel diameter D, both simulation and experiment with dsDNA reveal nonuniform mixing of the two chains, with one chain dominating locally in what we term "aggregates." Aggregates undergo stochastic dynamics, persisting for a limited time, then disappearing and reforming. Whereas aggregate-prone mixing occurs immediately at sufficiently high flow speeds, chains stay segregated at intermediate flow for some time, often attempting to mix multiple times, before suddenly successfully mixing. Observation of successful mixing nucleation events in nanofluidic experiments reveal that they arise through a peculiar "back-propagation" mechanism whereby the upstream chain, closest to the barrier, penetrates and passes through the downstream chain (farthest from the barrier) moving against the flow direction. Simulations suggest that the observed back-propagation nucleation mechanism is favored at intermediate flow speeds and arises from a special configuration where the upstream chain exhibits one or more folds facing the downstream chain, while the downstream chain has an unfolded chain end facing upstream.

DOI: 10.1103/PhysRevE.109.024501

I. INTRODUCTION

Single confined polymer chains have a rich physical description. For example, several different confinement regimes exist for one-dimensional (1D) tubelike confinement alone, including de Gennes and extended de Gennes regimes for weak confinement with the channel width D larger than the chain persistence length P and the Odijk regime for $D \ll P$ [1,2]. When a second polymer chain is added, complicated mixing and demixing behavior arises with demixing enhanced in anisotropic (tubelike) confinement [3]. While systems of two confined polymers have been studied extensively, such studies are mostly limited to their equilibrium, ensemble-averaged states. Yet it is known that nonequilibrium, force-constrained single DNA chains in nanochannels exhibit striking transient behavior [4,5]. When a relaxed, extended DNA chain inside a nanochannel is pushed by a piston sliding down the channel at fixed speed, the piston sends shockwaves down the chain during compression; once the piston is removed, the chain gradually relaxes back into its equilibrium state. Simulations of polymer chains under piston compression show a deterministic, predictable folding of the chain over time, with the timescale determined by factors such as persistence length, channel size, and piston speed [6]. Behaviour similar to the piston compression experiment can be observed by applying hydrodynamic flow down the channel that compresses the polymer against a flow-permeable barrier in the channel, which blocks the polymer but lets buffer pass through a thin slit. The flow-induced compression experiment is equivalent to the piston experiment, differing through a change of reference frame. However, it is much easier to achieve experimentally as channel dimensions and flow speed can be fine tuned while an optical tweezer controlled piston is limited in the range of force it can apply as well as the size of the channel it can operate in.

When this flow-induced compression is applied to a system of two nanochannel-confined polymers, behavior much more subtle than mere mixing and segregation can occur [7]. For stiff chains with a persistence length P greater than the channel diameter D, molecular dynamics (MD) simulations show that mixing and demixing depend largely on intrachain organization. In particular, mixing is partial or complete at low compressive flow because both chains are in hairpin fold configurations, in which they occupy little channel cross-section area, so they can easily coexist side by side. At high flow, chains are in a mostly coiled configuration, where each coil occupies a much larger cross-section area than a fold, so, when initialized in a segregated state, the chains remain mostly demixed, with more coiling correlated with more demixing. For less stiff chains ($P < D$), while coiling and folding are still present, mixing is no longer smooth: each chain forms locally what we term "aggregates", by which we mean that the chain will transiently cluster and have its local concentration dominate over the other chain for a portion of the length of the packed chain along the channel. Aggregates can persist for some time, but typically diffuse, disappear, and reappear in a stochastic fashion. Aggregation becomes more pronounced and less time persistent for completely flexible chains. In addition we observe that mixing arises via a nontrivial transient dynamics. For $P < D$, when initially segregated chains are placed under flow-induced compression, the chains do not mix immediately, but only after a certain waiting time.

*lili.zeng@mail.mcgill.ca
†reisner@physics.mcgill.ca

The mixing then spontaneously nucleates, the two chains transitioning to a mixed state where they overlap almost completely, but with alternating aggregates where one chain locally dominates. Mixing nucleation has also been observed in nanofluidic experiments where two dsDNA molecules in nanochannels are compressed via applied hydrodynamic flow [8].

Here we use molecular dynamics (MD) simulations, supported by nanofluidic experiments, to probe in detail the nonequilibrium mixing and demixing dynamics of two nanochannel-confined polymer chains in a flow field. We find for intermediate flow speeds most relevant for experiments that mixing nucleation proceeds through a curious and non-intuitive dynamics that we term "back-propagation." The two chains spontaneously adopt a particular initial configuration where the upstream chain (furthest from the barrier) exhibits one or more folds facing the downstream chain (closest to the barrier), while the downstream chain has an unfolded chain end facing upstream. When mixing initiates, the two chains will begin to overlap, but nonuniformly: a portion of the downstream chain will penetrate through the upstream chain *moving against the direction of flow*, i.e. "back-propagating," until the downstream chain completely slips past the upstream chain. While the intrachain configuration is not accessible in nanofluidic experiments with DNA, due to optical resolution limits, we observe very similar overall chain conformations as seen in simulation. In particular, we observe aggregate-prone mixing and back-propagation dynamics in our experimental data. Coarse-graining the simulation and experimental data reveals that back-propagation is a common feature of the two chain state dynamics.

II. METHODOLOGY

A. Model and simulation details

Our simulations are performed using the MD package ESPRESSO [9] using a bead-spring model of a polymer with the monomers interacting via excluded volume, a finite extension nonlinear elastic spring potential, and a bond-bending potential to model semiflexibility ($P \neq 0$) [7,10]. We keep the channel width D, the monomer size σ, the number of monomers per chain $N_1 = N_2 = N$, and the chain persistence length P (when simulating semiflexible chains) fixed, but vary the flow speed v to explore chains subject to different flow velocities. The excluded volume interaction between any two monomers from either chain, separated by a distance of r, is given by a short-range truncated Lennard-Jones (LJ) potential, also called the Weeks-Chandler-Andersen (WCA) potential [11]:

$$U_{WCA}(r) = 4\epsilon\left[\left(\frac{\sigma}{r}\right)^{12} - \left(\frac{\sigma}{r}\right)^{6} + \frac{1}{4}\right] \quad \text{if } r < 2^{1/6}\sigma$$
$$= 0 \quad \text{otherwise,} \qquad (1)$$

where ϵ is the interaction strength. The successive monomers of each chain are connected by a finite extension nonlinear elastic (FENE) spring potential [12]:

$$U_{\text{FENE}}(r) = -\frac{1}{2}kR_0^2 \ln\left(1 - \frac{r^2}{R_0^2}\right), \qquad (2)$$

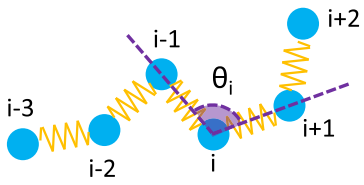

FIG. 1. Diagram showing a bead-spring model chain with the angle between bonds θ, from which the bending energy is calculated.

where k is the interaction strength and R_0 is the maximum allowed bond length. The parameters k, R_0, ϵ, and σ determine together the average bond length. The chain stiffness is controlled by a three body cosine bond-bending potential:

$$U_{\text{bend}} = \kappa[1 - \cos(\theta - \theta_0)], \qquad (3)$$

where θ, shown in Fig. 1, is the angle between two successive bonds, κ is the interaction strength, and θ_0 is the equilibrium bond angle. For $\kappa \neq 0$, the persistence length P of the chain is related to κ via [13]

$$P = \frac{\kappa\sigma}{k_BT}, \qquad (4)$$

where k_BT is the thermal energy. The confining walls of the cylindrical nanochannel, including both ends, interact with monomers also via the WCA potential, but with interaction strength $\epsilon_{\text{walls}} = 20\epsilon$ and interaction length $\sigma_{\text{walls}} = 0.2\sigma$. As for the homogeneous applied flow field, it is defined by a force on each monomer,

$$\vec{F}_i = -\gamma_v(\vec{v} - \dot{\vec{r}}_i), \qquad (5)$$

where γ is the friction factor, $\dot{\vec{r}}_i$ is the velocity for monomer i and $\vec{v}$ is the flow velocity with $\vec{v} = (v_x, v_y, v_z)$, where $v_x = v$ and $v_y = v_z = 0$. Our model assumes a uniform flow profile, equivalent to polymer compression via sliding gasket in the frame of reference moving with the gasket. While pressure-driven flow would give rise to a parabolic flow profile, which our current model does not include, experiments implementing pressure-driven flow to compress nanochannel confined DNA [14] gave results comparable to sliding gasket experiments [4] in terms of the compressed chain packing and how the packing scales with flow and gasket translation speed. We believe that, in parabolic flow, a cross section of chain transverse to the channel axis mainly feels the flow force averaged over the channel cross section, so that the effect of the nonuniform flow profile is primarily to renormalize the imposed forcing by averaging over the nonuniform flow profile. In addition, there are no hydrodynamic interactions included in the simulations as they are expensive to compute, and their effect can be taken into account by normalizing the friction factor [6].

The MD simulation propagates forward using the Langevin equation of motion. For monomer i,

$$m\ddot{\vec{r}}_i = -\vec{\nabla}(U_{\text{WCA}} + U_{\text{FENE}} + U_{\text{bend}} + U_{\text{WCAwall}}) - \vec{F}_i + \vec{R}_i(t), \qquad (6)$$

where m is the monomer mass, r_i is the monomer position, γ is the friction coefficient, and $\vec{R}_i$ is a Gaussian random force that satisfies $\langle \vec{R}_i(i) \cdot \vec{R}_j(t') \rangle = 2d\gamma k_BT\delta_{ij}\delta(t - t')$ for thermal energy k_BT and in d dimensions [15].

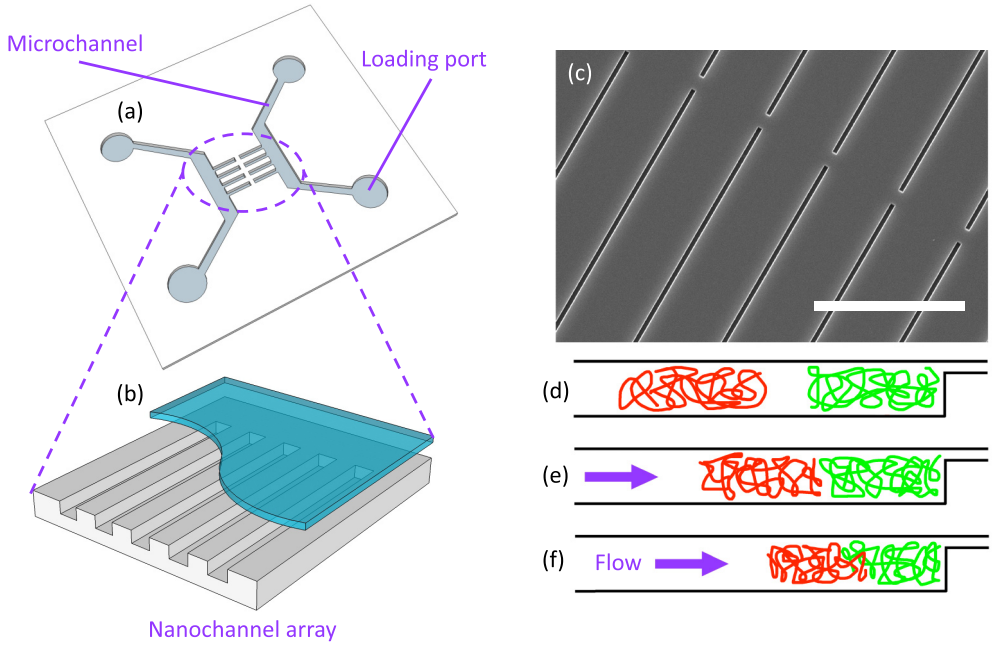

FIG. 2. (a) Schematic of our nanofluidic chip, where microchannels and loading ports where DNA solution is introduced are indicated. (b) Closer view of the nanochannel array. (c) SEM view of the nanochannel array on an actual chip where scale bar indicates 10 μm. [(d)–(f)] Drawings of cross sections of nanochannels showing the steps involved in an experiment, with DNAs being introduced into the channel (d), flow being applied (e), and compression being initiated (f).

For all our simulations, we set $\sigma = 1$, $N = 150$, $D = 6$, $m = 1$, $\gamma = 1$, and $k_BT = 0.2$. For the WCA potential, we set $\epsilon = 1$; for the FENE potential, we set $k = 10$ and $R_0 = 2$; and for the bending potential, we set $\theta_0 = \pi$. We use $\kappa = 0.48$, corresponding to a persistence length of $P = 2.4 < D$. We also perform simulations with no bending energy, or $P = 0$. Finally, we vary v [$\vec{v} = (v, 0, 0)$] by four orders of magnitude, between 0.00025 and 0.2.

For a given simulation run, we initialize two polymers consecutively in a straight line along the axis of the cylindrical channel. We set a fixed amount of time for the system to reach equilibrium ($t = 1 \times 10^6$, corresponding to 2×10^8 iterations of $\Delta t = 0.005$ each). We ensure that equilibrium and chain separation are reached by observing when the extension of both chains stabilizes and no chain portion overlaps in any given channel cross section perpendicular to the channel axis. We then apply the homogeneous flow field to compress the chain (for at least $t = 1 \times 10^6$). We run such simulations both with and without κ, and over 13 flow velocities v, with three independent simulation runs for each set of parameters, for a total of 78 runs of up to five days each. These simulations were run on Compute Canada's supercomputer cluster *Beluga*.

B. Fabrication process and experimental methods

Our nanofluidic devices, shown in Figs. 2(a) and 2(b), are fabricated in fused silica wafers (HOYA) using the protocol described in [2,14]. The nanochannels have rectangular cross section, of dimensions 300 nm × 600 nm, and are patterned in a double array separated by blunt ends in the chip center, as in Fig. 2(c). A 25-nm-deep slit is subsequently etched over the nanochannel double array, to allow for buffer flow while trapping the DNA. Adjoining each nanochannel array is a U-shaped microchannel (1 μm deep, 50 μm wide); these microchannels convey molecules from sand-blasted loading holes to the nanochannels. The fused silica chips are then bonded directly to fused silica coverslips, sealing the channels and the slit. Compression experiments are conduced with T_4 bacteriophage DNA (Nippon Gene, 166kbp). One chain is stained with YOYO-1 while the other chain is stained with YOYO-3. In both cases the staining ratio is set to 10:1 bp:fluorophore. The stained DNA solutions are diluted to 2.5 μg mL^{-1} in 10 mMol Tris prior to the experiment and β-mercaptoethanol at 2% is added as an antinicking and antibleaching agent. We mount the device on a chuck fabricated by a stereolithography 3D printer from Formlabs with Formlabs standard clear resin, with the loading ports connected to a nitrogen gas controller via luer connectors and sealed using a rubber gasket. The chuck-chip system is then mounted on an inverted microscope (Nikon Eclipse Ti-E) with a 100× numerical aperature 1.5 oil immersion objective, which is connected to an Andor iXon X3 EMCCD camera. In order to perform two-wavelength fluorescence imaging, we use an LED based two-color excitation system triggered externally by the exposure signal [16].

During a typical experiment, a solution containing both YOYO-1 and YOYO-3 stained DNAs are added into one loading port of each U-shaped microchannels, while pure buffer is loaded into the other. We apply pneumatic pressure from the gas controller to the loading ports containing DNA to drive the DNA molecules into the microchannels. Once a particular DNA molecule is selected for an experiment, we bring it to the entrance of a nanochannel by applying pneumatic pressure to one or the other loading port (for forward and backward movement along the microchannel), then apply pressure to both

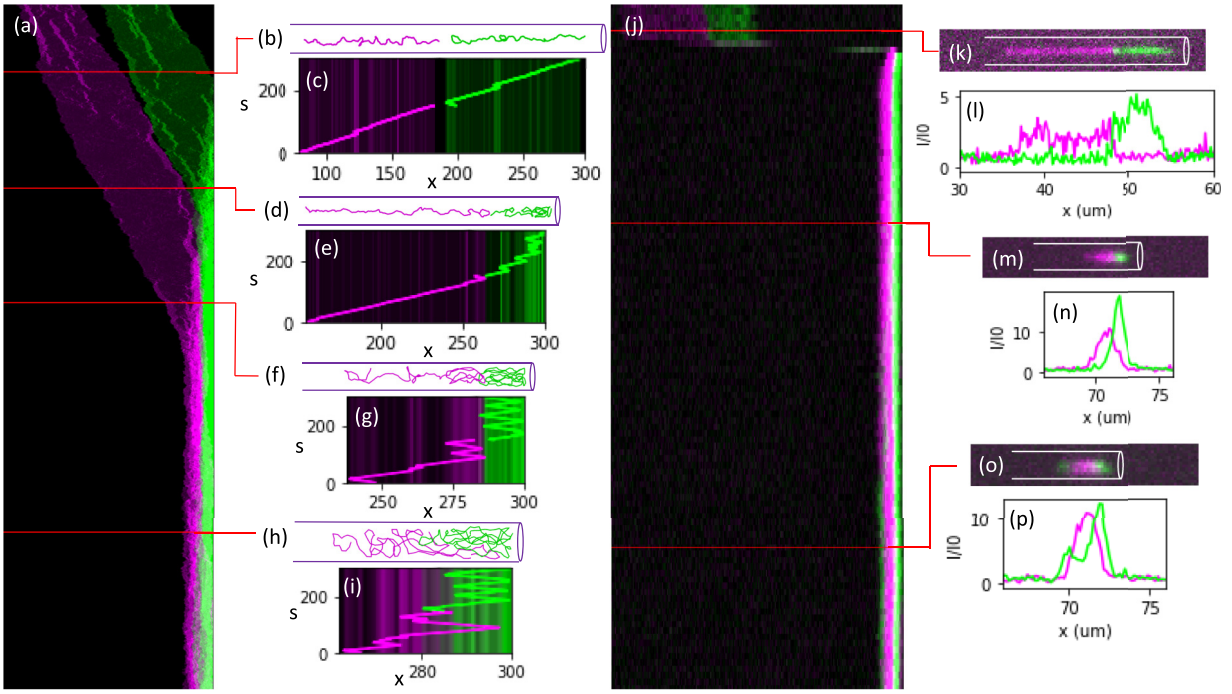

FIG. 3. (a) Typical kymograph for a simulation run, where (b), (d), (f), (h) are instantaneous snapshots of intrachain configuration and (c), (e), (g), (i) are corresponding longitudinal position plots. (j) Typical kymograph for an experimental run, where (k), (m), (o) are instantaneous snapshots as viewed under the microscope, and (l), (n), (p) are corresponding concentration plots.

ports to drive it into the nanochannel. We repeat the process with a second DNA molecule of contrasting stain. Once both differentially stained DNAs are in the nanochannel [Fig. 2(d)], we let them relax to their equilibrium extension (∼15 μm each), then apply pressure to the buffer-only port to compress the two DNA molecules against the barrier [Figs. 2(e) and 2(f), while being careful to not accidentally introduce new molecules into the nanochannel]. We record the compression event with each DNA imaged in alternating frames, at 5 frames/s, for a total event time ranging from 30 seconds to over 2 minutes. We then compile the resulting video by combining two consecutive separately taken images of each DNA into one composite frame. We repeat the experiment with fresh molecules once the initial set of molecules start to photobleach.

III. RESULTS

We use kymographs to display the time evolution of the local concentration of each chain as a function of position along the channel axis. A typical kymograph from simulation is shown in Fig. 3(a) while a typical kymograph from experiment is shown in Fig. 3(j). In order to obtain local chain concentrations from simulation, we divide the channel into discrete bins along the channel axis and obtain the number of monomers per each bin. Monomers from each of the two chains are counted separately and the concentrations of the two chains are rendered in separate colors (green and magenta). For experiments, kymographs are constructed by averaging the pixel intensity (separately for each color) for each frame along the direction transverse to the channel axis, and plotting these intensities row by row over time. Note that for all kymographs in this paper, from simulation or experiment, flow points towards the right.

We can see in Fig. 3 that the chains are always initialized in extended and nonoverlapping conditions, with a full configuration snapshot shown in (b) and microscopy snapshot in (k). As the chains are compressed [moving towards the right in kymographs (a) and (j)], chain overlaps appear as a regions on the kymograph that are of colors intermediate between green and magenta (i.e., greyish or whitish), with the color of the majority chain dominating.

We introduce longitudinal position vs monomer number plots for our simulation data, which are shown in Figs. 3(c), 3(e), 3(g), and 3(i). Each consecutive monomer of each chain is given an integer label s ranging from 1 to 300 (there are two chains of 150 monomers each). The longitudinal position vs monomer number plots give the monomer number s (vertical axis) vs the corresponding monomer position along the channel axis x (horizontal axis). The longitudinal position plots make the overall configuration of the two chains transparent, in particular with folds represented as kinks [Figs. 3(e), 3(g), and 3(i)].

We can also obtain chain concentration snapshots, shown in Figs. 3(l), 3(n), and 3(p) from simulation by plotting the local monomer concentration of each chain against the position along channel axis (in other words, a single kymograph row is plotted).

A. Aggregate-prone mixing

Figures 4(a)–4(e) give examples of kymographs for simulated semiflexible chains ($0 < P < D$) in steady-state and

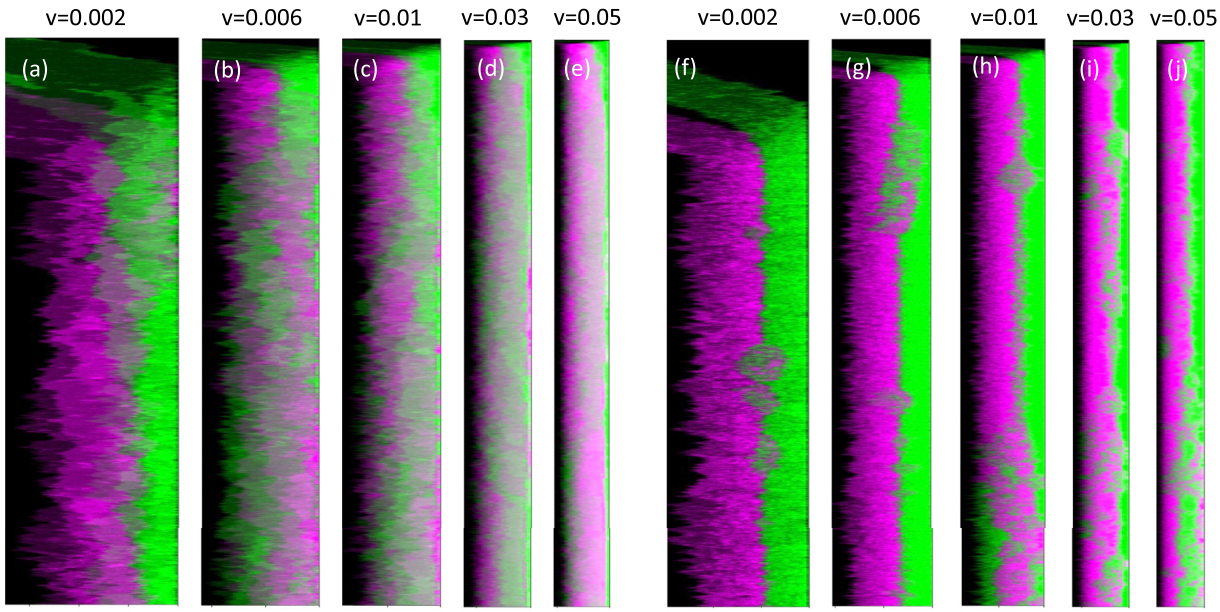

FIG. 4. [(a)–(e)] Typical simulation kymographs for semiflexible chains with $D/P = 2.5$, where $v =$ (a) 0.002, (b) 0.006, (c) 0.01, (d) 0.03, and (e) 0.05. [(f)–(j)] Typical simulation kymographs for flexible chains where $v =$ (f) 0.002, (g) 0.006, (h) 0.01, (i) 0.03, and (j) 0.05.

increasing flow speeds v. We can see that while there is mixing, the mixing is not uniform, with intermittent regions of green (chain 1) and pink (chain 2). These single-chain dominated areas are what we term aggregates. We can see that they spontaneously arise, persist for some time, diffuse, and then disappear. Note that at sufficiently high v the two chains will segregate, as discussed in our previous study (Zeng *et al.* [7]). The two chains are segregated before compression, and the flow is sufficiently high that whichever chain arrives at the barrier first will remain there, with positional fluctuation of the chain's center point suppressed by the high flow. Example kymographs for simulated flexible chains ($P = 0$) are shown in Figs. 4(f)–4(j). For flexible chains we observe a decrease in mixing compared to the semiflexible case. Almost every position along the packing has one chain strongly dominating over the other. We also observe that the aggregates persist for a shorter time and diffuse more rapidly. Examples of kymographs for real dsDNA chains in rectangular nanochannels of cross section 300 nm × 600 nm are shown in Fig. 5, for flow speeds around 20 μm/s. We observe aggregates, as in our simulations.

We argue that aggregates arise via entropic demixing [3]. Two chains in a tubelike, anisotropic confinement will have more conformational freedom if they each occupy a portion of the tube (segregated), rather than if they are squeezed side by side in the tube (mixed). Similarly, in our case, while flow pushes the chains to mix, the mixing is not complete because entropy is maximized if one chain is locally dominant. A sketch showing a comparison of aggregation vs complete mixing is shown in Figs. 6(a) vs 6(b). We can see that at the location of an aggregate, one chain gives up its conformational freedom completely (by remaining almost completely straight), while maximizing the conformational freedom of the other chain. This aggregation effect is expected to be more pronounced for flexible chains compared to semiflexible chains, as flexible chains have no energy penalty in bending sharply to form tighter aggregates. This effect is observed in our simulation results [Figs. 4(a)–4(e) vs 4(f)–4(j)].

We explore the statistics of aggregate sizes in Fig. 7 for simulated semiflexible chains. For each frame, or row of a kymograph, we define an aggregate as consecutive points along the kymograph where one chain has higher concentration than the other. The size of the aggregate is then the number of consecutive points it spans. We then histogram the aggregates by size over all selected frames and all runs with the same flow speed. We observe an exponential decay (highlighted by the black dash line) at large aggregate sizes. This behavior is consistent with an aggregate free energy decrease relative to the unaggregated chains scaling linearly with aggregate length, as predicted by entropic demixing. Note that we include only frames after mixing has occurred (after the first successful mixing nucleation, which is defined in the next subsection) in the histograms.

B. Nucleation of mixing

At high flow speeds, aggregate-prone mixing arises immediately upon compression; at very low flow speeds, mixing is absent (especially for flexible chains). For simulations at intermediate flow speeds a distinct phenomenon arises: the two chains are initially segregated, then mixing spontaneously "nucleates" with the time to mixing showing stochastic variation between compression events. Upon closer inspection, there are often multiple mixing nucleation attempts, but only once or twice are attempts "successful" (leaving the two chains visibly mixed thereafter). Figures 8(a), 8(d), 8(g), and 8(i) show example kymographs for semiflexible chains, where mixing nucleation attempts are indicated by the white lines. Figures 8(b), 8(e), 8(h), and 8(k) show reduced kymographs, where regions with only chain 1 or chain 2 are present are shown in green and pink respectively, regions with both chains present are shown in grey, and empty regions are shown

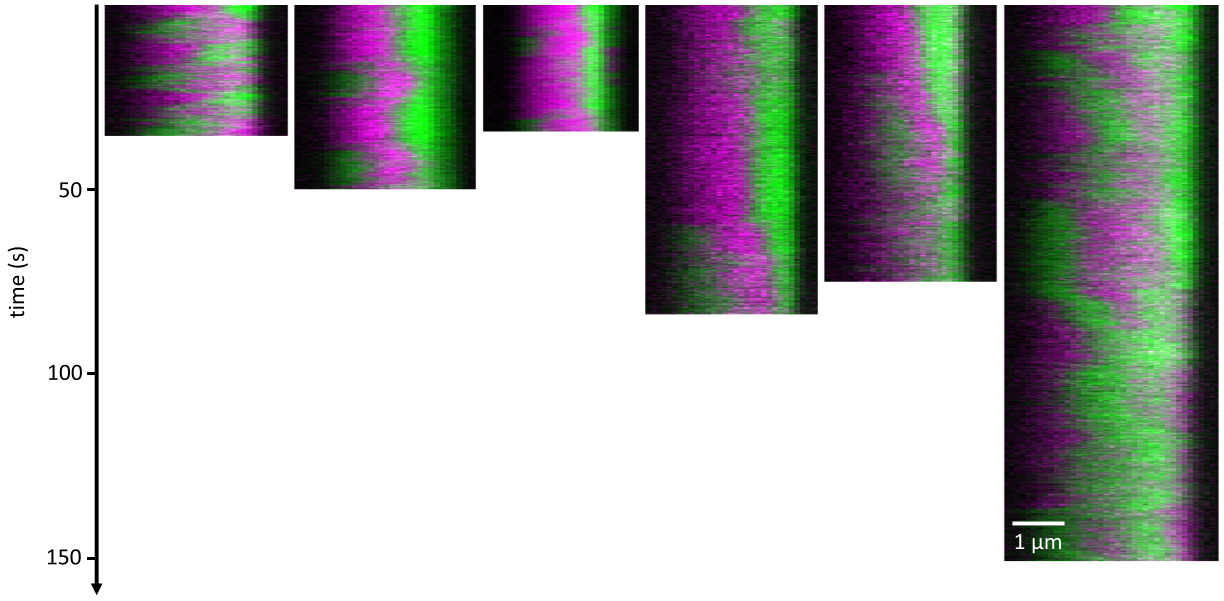

FIG. 5. Kymographs for nanofluidic experiments of dsDNA in nanochannels.

in black. The reduced kymographs better delineate regions where mixing and segregation occur.

Using the reduced kymograph, we can compute frame by frame the ratio of the extension of the mixed (grey) region over the whole extension of the two-chain packing (green + grey + pink), plotted in Figs. 8(c), 8(f), 8(i), and 8(l). This mixing ratio fluctuates significantly due to random fluctuations in configurations, so we smooth it by computing its rolling average value over 50 frames. The mixing ratio takes values between 0 and 1, with low values indicating more segregation and high values indicating more mixing. We then define mixing nucleation as whenever the mixing ratio increases beyond a threshold (plotted in red), which we set as 0.2 for semiflexible chains. This threshold is chosen as it corresponds visually with where mixing occurs in the reduced kymographs [see reduced kymographs in Figs. 8(b), 8(e), 8(h), and 8(k)]. When the mixing ratio crosses the 0.2 threshold and then crosses a higher 0.5 (plotted in blue) threshold without dipping below 0.2, we consider this to be a successful nucleation event.

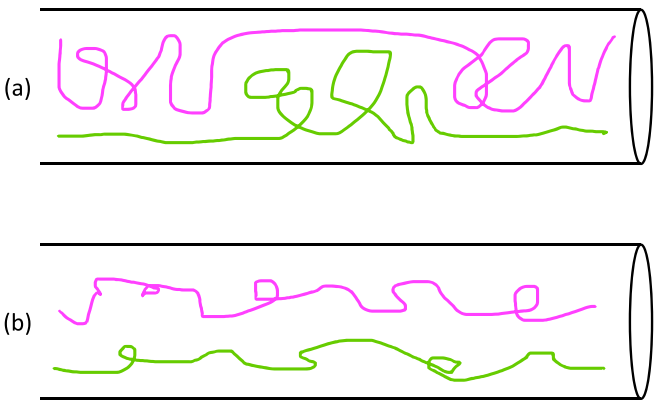

FIG. 6. (a) Sketch showing two chains exhibiting aggregated mixing. (b) Sketch showing two chains mixing smoothly.

While mixing nucleation is less obvious in kymographs of flexible chains [Figs. 9(a), 9(d), 9(g), and 9(i)], the reduced kymographs [Figs. 9(b), 9(e), 9(h), and 9(k)] help visualize the nucleation events. We can similarly plot the mixing ratio [Figs. 9(c), 9(f), 9(i), and 9(l)], but the thresholds are set to 0.3 and 0.5 instead [again, to correspond to when visually a mixing nucleation occurs in the reduced kymographs; see Figs. 9(b), 9(e), 9(h), and 9(k)]. Note that, for both flexible and semiflexible chains, mixing nucleation happens increasingly later in the simulation run for increasingly low flow speeds, as expected.

The presence of mixing nucleation prompts the question, what causes the chains to suddenly mix, when they were previously segregated? The answer is revealed when plotting the intrachain configurations during these nucleation events. Figure 10 shows one such event for semiflexible chains. With the region of the mixing nucleation highlighted in the kymograph in (a), we observe in (b)–(g) a segment of the green chain passing through the folded pink chain (with movements indicated in yellow arrows in the longitudinal position plots) before ultimately appearing at the other end of the packing.

A flexible chain exhibiting this phenomenon twice in a run is shown in Fig. 11. Again, each event is highlighted in the kymograph in (a), and we observe in each case [(b)–(f) and (g)–(k)] a segment of the green chain being inserted through a group of several folds in the pink chain. Note that the timescale of the nucleation event is much shorter compared to the semiflexible case.

While intrachain configuration is not available, we observe the same kind of behavior in experiments. We plot instead chain concentration as a function of position along the channel axis. We show an example event of experimental concentration snapshots for each chain, frame by frame, in Figs. 12(l)–12(p), with corresponding kymograph in (a). For comparison, we show simulation data for flexible chains plotted the same way in (g)–(k). We also plot the corresponding longitudinal position plots to (g)–(k) in (b)–(f). We see a small

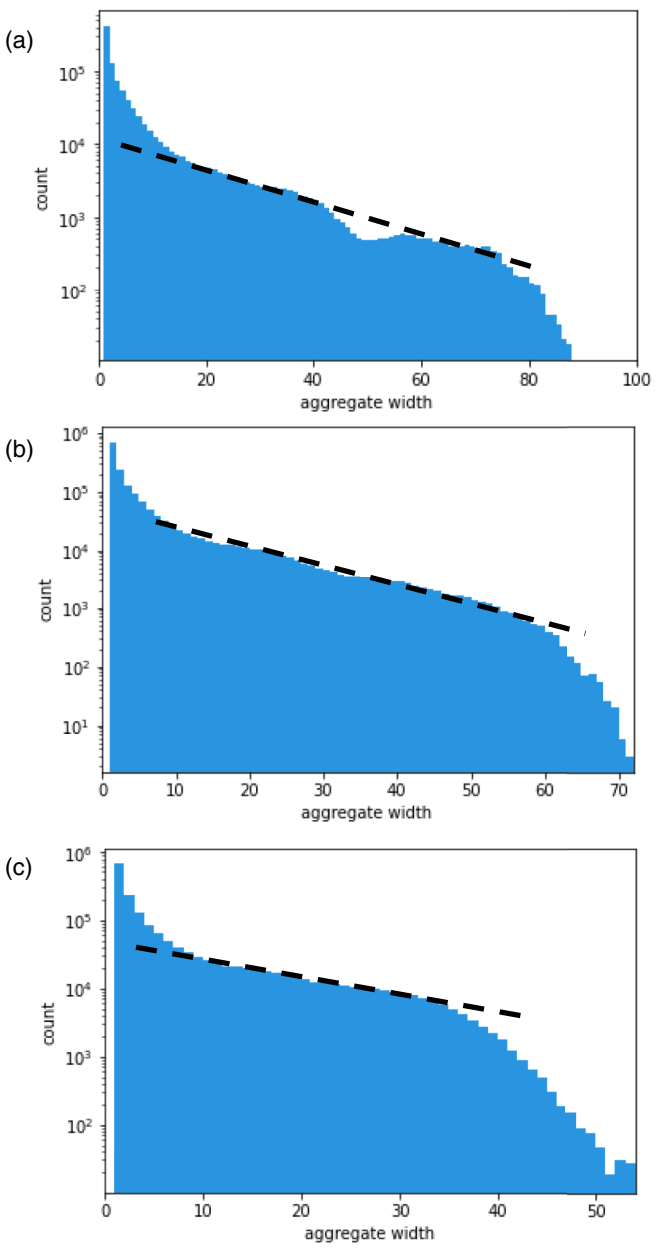

FIG. 7. Histogram of aggregate sizes for simulated semiflexible chains at v = (a) 0.0005, (b) 0.001, and (c) 0.002, with exponential decay indicated in black dash. Note that histograms are truncated at an aggregate width equal to the average length of the two chain packing. As the aggregate width cannot exceed the length of the two chain packing, we expect the number of aggregates to depart from the exponential scaling as the aggregate width approaches this maximum length, especially at the lowest flow speed where the chains overlap less, and therefore aggregate sizes do not even approach the packing size.

portion of the green chain "back-propagating," penetrating through the pink chain to pop out on the other side in both simulation and experiment.

We hypothesize that mixing nucleation is favored when a folded region of the upstream chain (further from the barrier) faces an extended segment in the downstream chain (closer to the barrier). Mixing arises more easily for this special configuration because it lowers the free energy barriers for nucleation. Folds in the upstream chain contain more contour than the extended portion of the downstream chain. The flow then pushes the folds forward more strongly, while the downstream chain strand occupies less channel cross-section area than the folds, so it does not obstruct the forward movement of the folds. As a result, the upstream folds are driven forward while the downstream chain loses contour to the extended segment penetrating the upstream stream. This extended downstream segment then travels countercurrent through the upstream chain and emerges at the end of the packing away from the channel end.

Is this configuration responsible for all mixing events? While this configuration is observed in experiments when successful mixing nucleation occurs, simulations reveal a more complex picture. Simulations suggest mixing nucleation can occur via other pathways at low and high flow speed, but the back-propagating configuration is critical for successful mixing nucleation at intermediate flow speeds, where chains are mostly folded but mixing is observed with a long stochastic delay. Figure 13(i) shows four possible configurations for the adjacent regions of the upstream and downstream chain. In configuration 1, the upstream chain is an extended strand conformation while the downstream chain is folded. In configuration 2, the downstream chain is an extended strand conformation while the upstream chain is folded; this corresponds to the back-propagating configuration. In configuration 3 both upstream and downstream chains are folded, and in configuration 4 both chains are extended. The configuration classification presents a challenge for flexible chains, due to the presence of many small local folds that makes the folding state less defined. For these configurations to apply to flexible chains, we must ignore small local folds (i.e., a chain is considered to be exhibiting a tail as long as the furthest monomer is within n monomers of a chain end; we set $n = 5$ for semiflexible and $n = 10$ for flexible chains).

In Fig. 13, we compile the configurations of all mixing nucleation events for (b) semiflexible and (f) flexible chains. Configuration 2 does not dominate. Instead, we see that at higher flows, configuration 3 dominates while at lower flows, configuration 4 dominates. At the lowest flows, the chains are almost completely extended when we look at intrachain configurations, and tend to encounter each other as such, hence the dominance of configuration 4 where tail faces tail. At the higher flows, there are more folds per chain, so the likelihood of folds encountering folds, or chains being in configuration 3, is higher. At the same time, higher flow reduces the barrier to mixing nucleation. With chains being mostly in configuration 3, and with mixing energy cost lowered, it is then evident that mixing attempts in configuration 3 will dominate. But what about configuration 2?

We plot only successful nucleation events in Fig. 13 for (d) semiflexible and (h) flexible chains. Again, we see that configuration 4 dominates at low flows and configuration 3 dominates at higher flows. However, configuration 2 dominates at a critical intermediate flow: $v = 0.0005$ for semiflexible chains and $v = 0.01$ for flexible chains. For the critical intermediate flows, mixing attempts in configuration 2 are not necessarily more likely, but they are more likely to be successful.

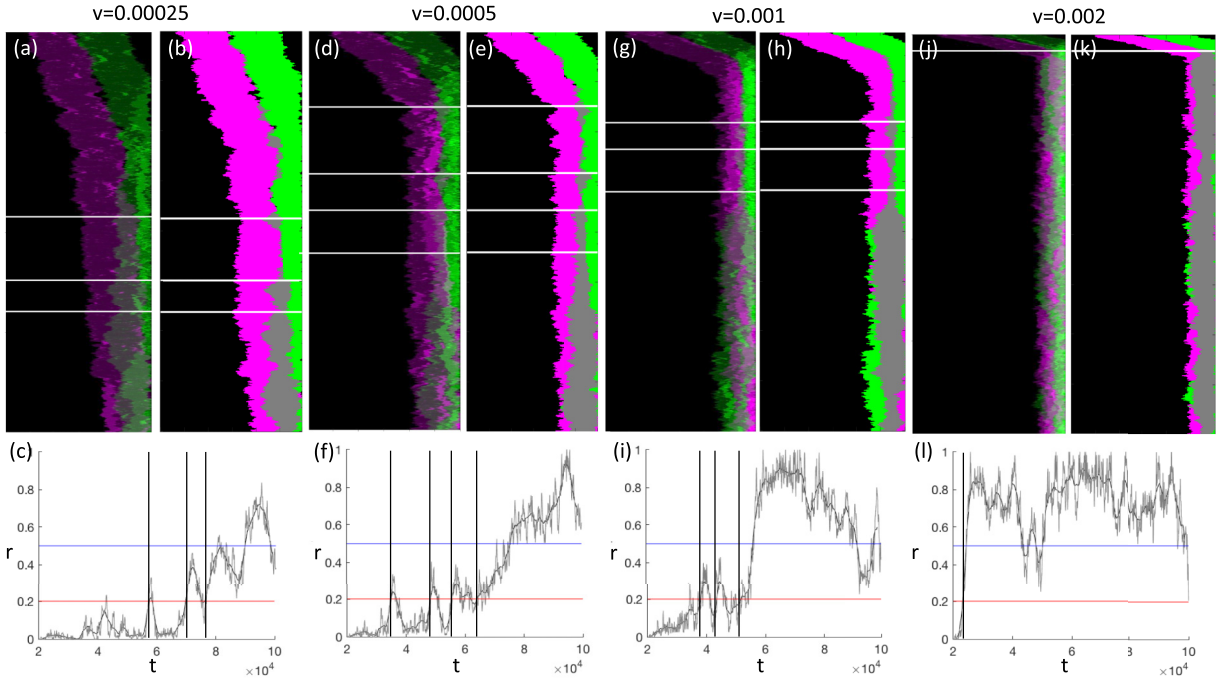

FIG. 8. (a), (d), (g), (i) Kymographs for simulated semiflexible chains, with mixing nucleation indicated by the white lines. (b), (e), (h), (k) Reduced kymographs with mixing nucleation indicated by white lines. (c), (f), (i), (l) Mixing ratio r (grey) and smoothed mixing ratio (black), with the 0.2 threshold in red and the 0.5 threshold in blue. Mixing nucleation times are shown by vertical black lines.

What is special about this critical intermediate flow? Let us focus on semiflexible chains and look at the average wait time of first mixing nucleation, plotted in Fig. 13(a), and at the total number of mixing attempts, plotted in Fig. 13(b) in black. We notice that mixing nucleations are more abundant at intermediate flows, and that the average wait time of first mixing nucleation decreases as flow increases. This is because at low flow the flow is too low to even induce many mixing nucleation, given the long time it takes for each mixing nucleation to happen. At intermediate flow speeds,

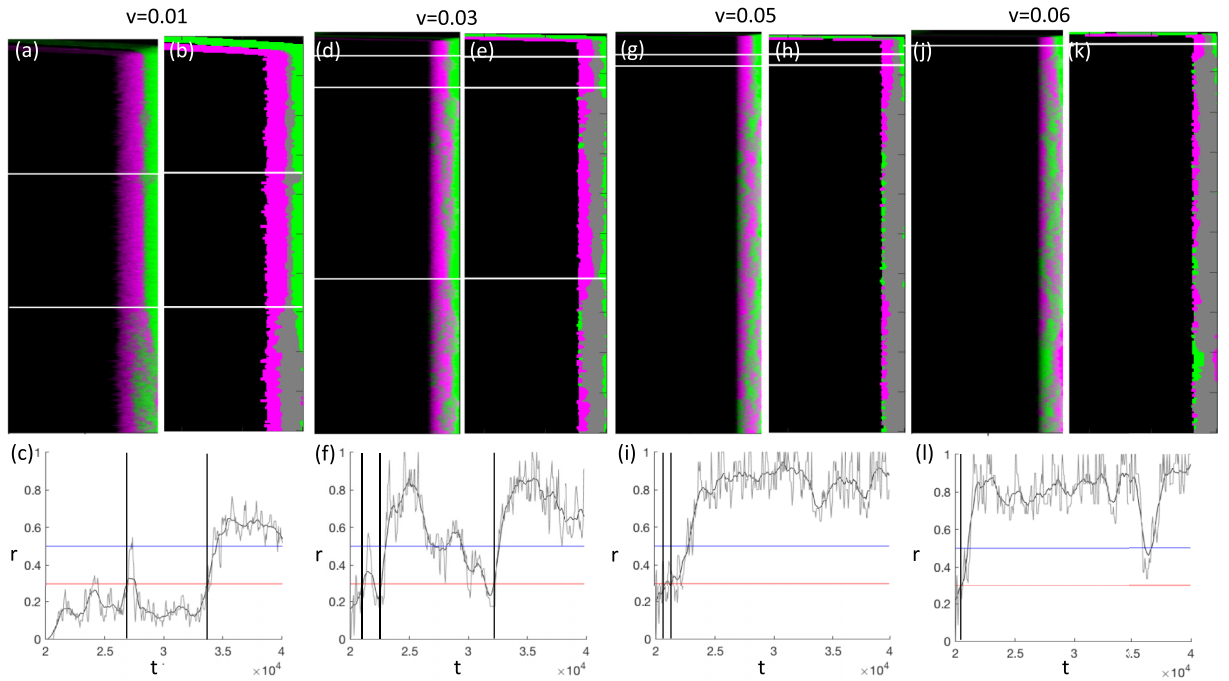

FIG. 9. (a), (d), (g), (i) Kymographs for simulated flexible chains, with mixing nucleation indicated in white lines. (b), (e), (h), (k) Reduced kymographs with mixing nucleation indicated in white lines. (c), (f), (i), (l) Mixing ratio r (grey) and smoothed mixing ratio (black), with the 0.3 threshold in red and the 0.5 threshold in blue. Mixing nucleation times are shown by vertical black lines.

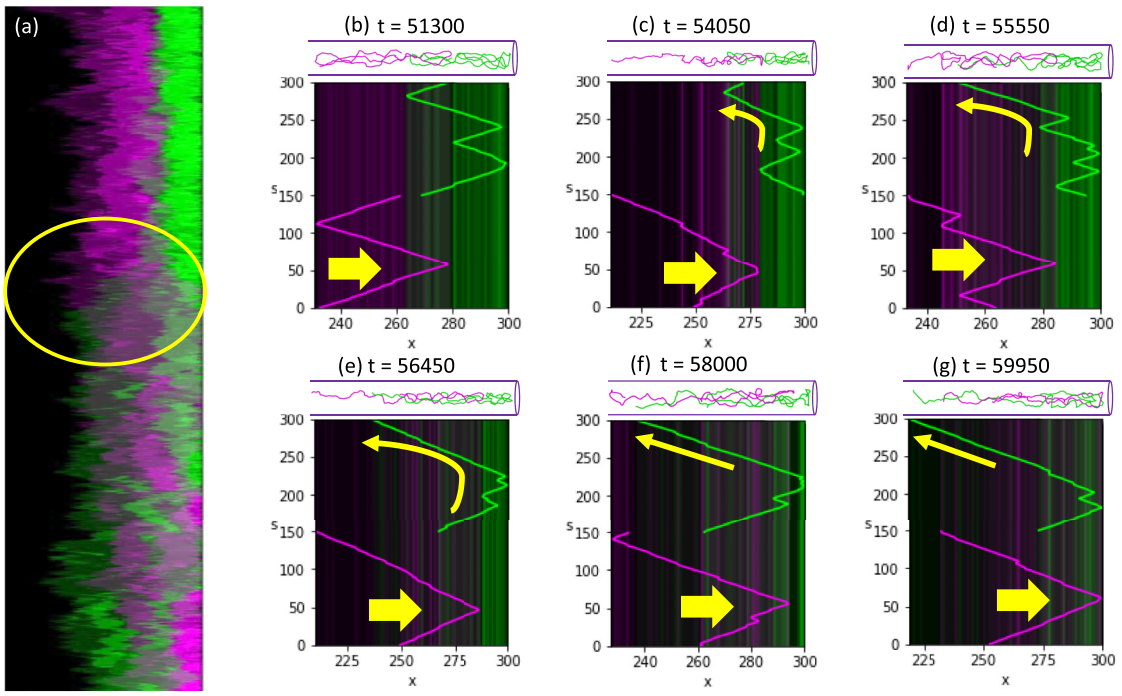

FIG. 10. (a) Simulation kymograph showing a nucleation event (circled in yellow) for semiflexible chains at $v = 0.001$, with [(b)–(g)] showing steps involved in the process with configuration snapshots and longitudinal position plots. A video of the event is available in the supporting information of the current paper.

mixing nucleation are more abundant, and it takes less time for them to happen. At highest flows however, mixing nucleations happen faster and are almost always successful, hence there are fewer of them in total. If we look at the average wait time of first successful mixing nucleation, plotted in Fig. 13(c), and at the total number of successful mixing attempts, plotted in Fig. 13(d) in black, we see that successful attempts number increases with flow speeds whereas the wait time of successful

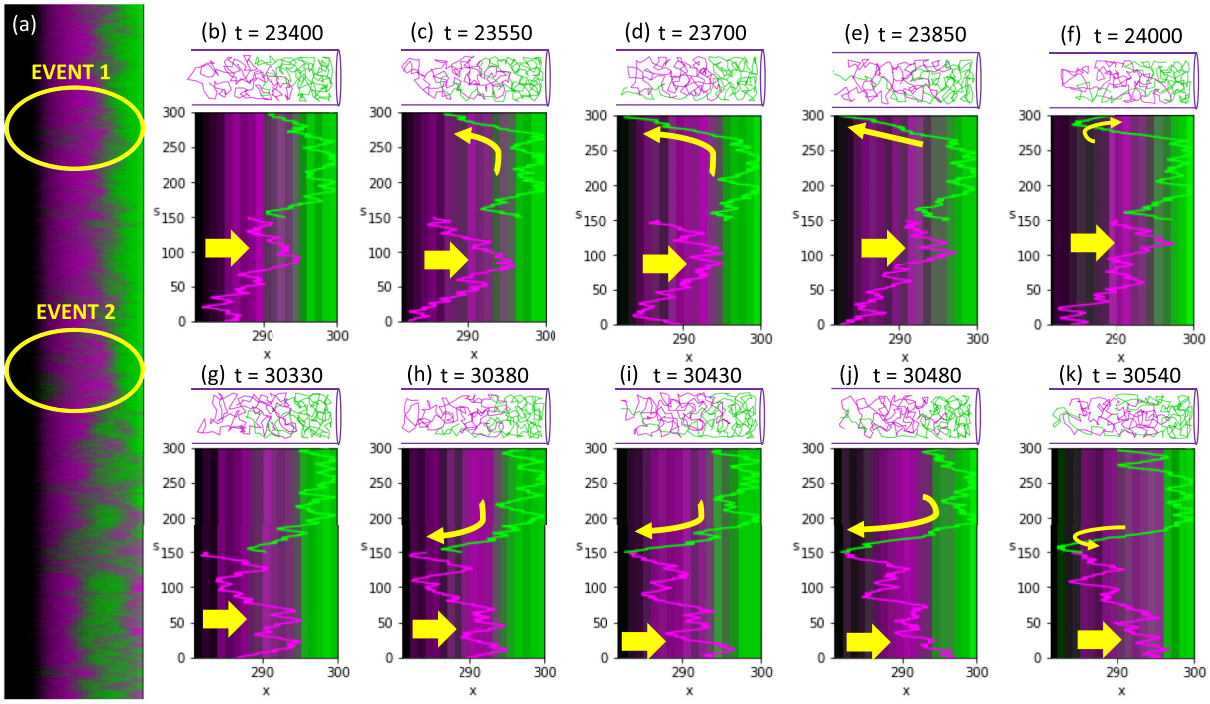

FIG. 11. (a) Simulation kymograph showing two nucleation events (circled in yellow) for flexible chains at $v = 0.05$, with [(b)–(f)] and [(g)–(k)] showing for each event the steps involved in the process with configuration snapshots and longitudinal position plots. Videos of the two events are available in the Supplemental Material [17] of the current paper.

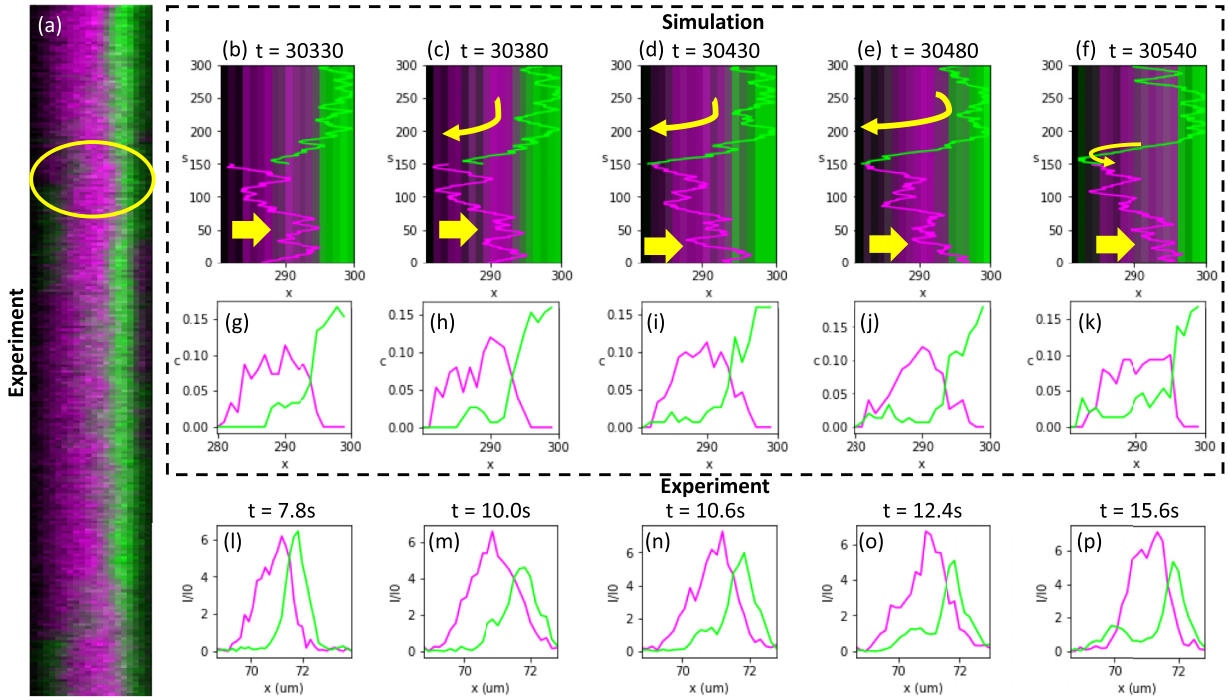

FIG. 12. (a) Experimental kymograph where a mixing nucleation event is indicated in yellow. [(b)–(f)] Comparison longitudinal plots for a similar simulation mixing nucleation event. [(g)–(k)] Comparison concentration plots for the same simulation mixing nucleation event. [(l)–(p)] Concentration plots for the experimental mixing nucleation event shown in (a).

mixing peaks at low and intermediate flow speeds. At low flow, chains are always extended and mix in an extended side-by-side configuration. At high flow, chains are folded, but mix readily because flow is sufficient to overcome the energy barrier. Only at the intermediate flow, the chain is folded, but the energy barrier is high. This is where the special configuration 2 is necessary for mixing to be successful. For flexible chains, we observe a similar trend to the semiflexible case [see Figs. 13(e)–13(h)], with the major difference being that all these mixing regimes occur at higher flow speeds.

C. Typical progression of mixing

In order to facilitate analysis of experimental data, for which only concentration plots are available, we coarse grain the concentration plots into seven states, as shown in Fig. 14(c). State 0 refers to when there is no mixing. States 1 to 3 shows the familiar progression seen in Figs. 12(l)–12(p). States 4 to 6 shows the same progression, but with the positions of green and pink chains swapped. Note that the difference between states 1 and 2, and also between states 4 and 5, lies in the one of the two chains that dominates in the overlap region. If the hypothesis that configuration 2 mentioned previously favors mixing nucleation, then in both simulation and experiments, we should observe frequent progression from state 1 to state 2 to state 3, because the green chain is initiated closer to the barrier, making states 1 and 2 the first states to be reached after initiating in state 0. We should also observe progression from state 4 to 5 to 6, but we expect fewer of those as state 4 can be reached only after state 3. Examples of such progressions are shown in Figs. 1 and 2 in the Supplemental Material [17].

A quantitative approach to understanding the two-chain state dynamics is to compute the transition probability matrix, where the value for row n and column m refers to the probability that any given frame of state n (one of the seven shown in Fig. 14) will transition to state m at the next frame. To present this data visually, we plot a few rows of the transition matrices in Figs. 15(a)–15(c) for simulated flexible and semiflexible chains and experiment. Note that the computed transition probabilities suggest nearest-neighbor transitions of the type $n \rightarrow (n+1)$ and $(n+1) \rightarrow n$ dominate, leading to progressions of the type $0 \rightarrow 1 \rightarrow 2 \rightarrow 3$. The probability of a $2 \rightarrow 1$ back-transition is higher than a $2 \rightarrow 3$ transition [Fig. 14(c)]; this reflects the difficulty of transiting to state 3 involving a molecule that extends through the packing length, the rate limiting step for completing back-propagation. Semiflexible simulation and experiment show qualitative agreement, with the exception of the stay probability for state 0 ($0 \rightarrow 0$). Note that the timescale of mixing in experiments is matched to simulation based on ensuring that the transition rates are comparable (see Supplementary Material [17]); this implies that comparing the relative transition rates of simulation and experiment in Fig. 14 is most meaningful (e.g., the ratio of the rates for $1 \rightarrow 2$ and $1 \rightarrow 0$, $2 \rightarrow 3$ and $2 \rightarrow 1$).

IV. DISCUSSION AND CONCLUSION

In summary, two low stiffness semiflexible chains ($0 < P < D$), confined in a nanochannel and subjected to a nonequilibrium flow field, exhibit nonuniform mixing with local aggregates appearing, diffusing, and then disappearing. We attribute the aggregation to entropic demixing, as

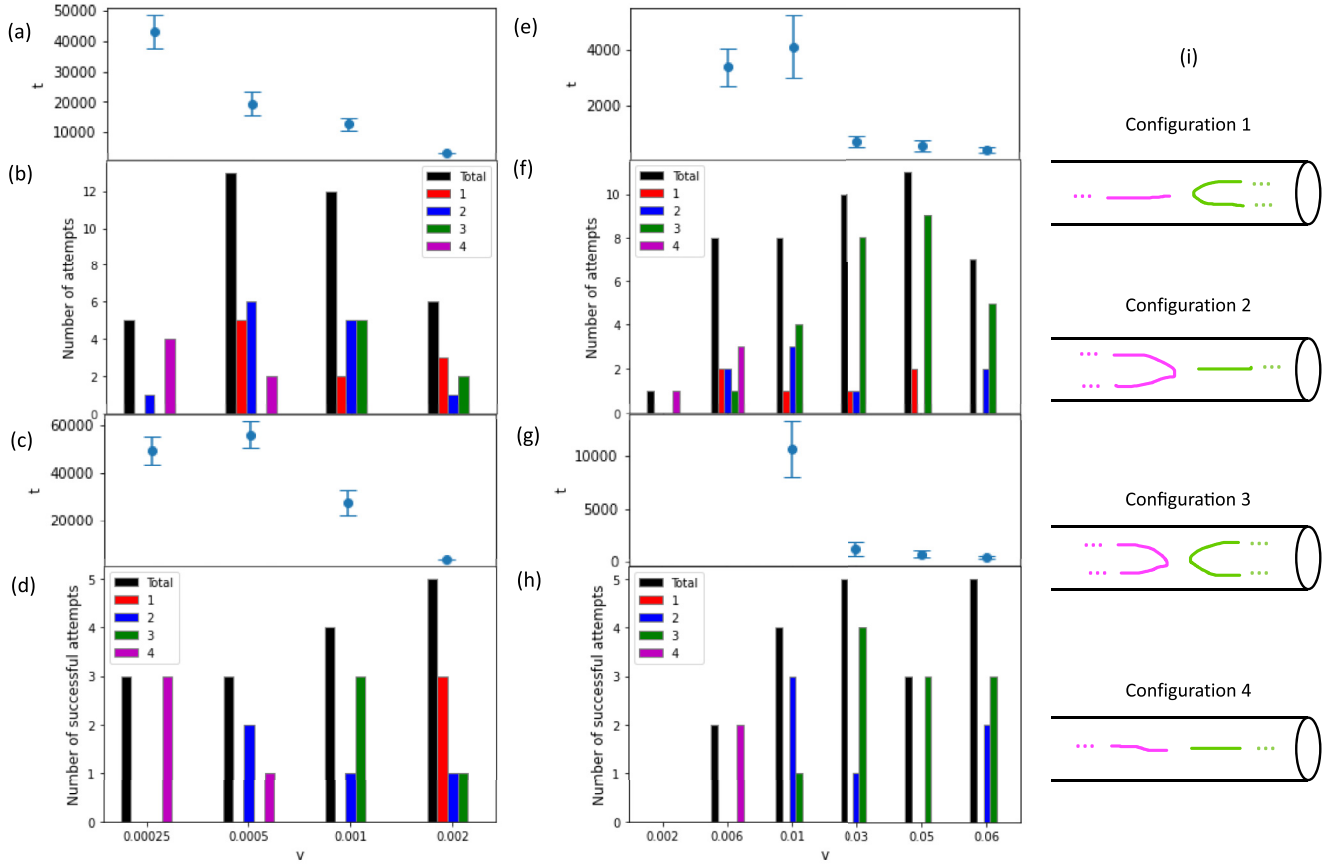

FIG. 13. Average wait time for first nucleation attempt for (a) semiflexible and (e) flexible chains. Number of nucleation attempts for different configurations for (b) semiflexible and (f) flexible chains. Average wait time for first successful nucleation attempt for (c) semiflexible and (g) flexible chains. Number of successful nucleation attempts for different configurations for (d) semiflexible and (h) flexible chains. [(a)–(h)] are simulation results. (i) Schematics of the four possible configurations.

suggested by the exponential decay of observed aggregates with aggregate extent. Two flexible chains ($P = 0$) exhibit more pronounced aggregates with fluctuations on a shorter timescale (by a factor of about 4). At sufficiently low flow speeds, flexible chains remain segregated (as if no flow is applied). At intermediate flows, flexible and semiflexible chains remain segregated only for a finite and variable time before mixing nucleates. Mixing nucleation is more successful when the upstream chain exhibits one or more folds facing the downstream chain, while the downstream chain exhibits an extended strand facing the upstream chain.

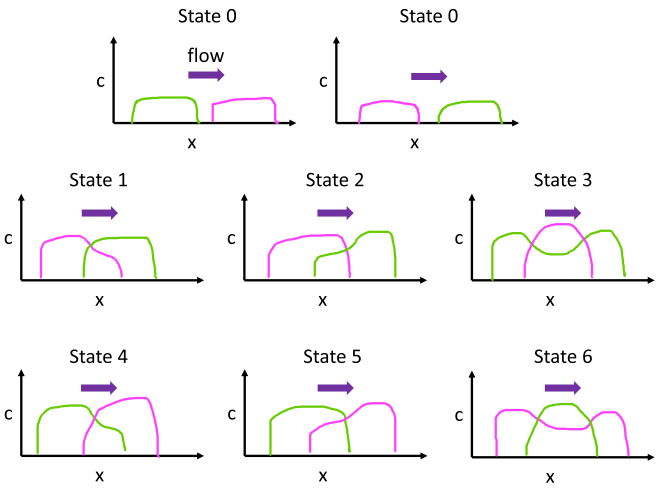

FIG. 14. Sketch showing coarse-grained states 0 to 6. Note that we always initiate the compression in state 0 with the green chain near barrier.

These observations hold true for simulation, but also for nanofluidic experiments, even though intrachain organization is not available due to optical resolution limits. In particular, we observe aggregate-prone mixing in DNA. We also observe "back-propagation" of the downstream chain through the upstream chain at low concentration, appearing as a third aggregate at the upstream end. This back-propagation indicates that most likely, the DNA chains are in the same configuration favourable to mixing simulated polymers. Further study of coarse-grained states supports this hypothesis in both simulation and experiments, demonstrating a common time progression in chain dynamics consistent with back-propagation.

Knotting and self-entanglement have been observed in single compressed chains, both experimentally [14,18] and in simulation [19,20]. Exploring how knotting and entanglement influences two chain compression is worth further investigation. Our previous study has found that knots continually form and unravel when two chains are compressed [7], and we expect similar behavior for entanglement between two chains.

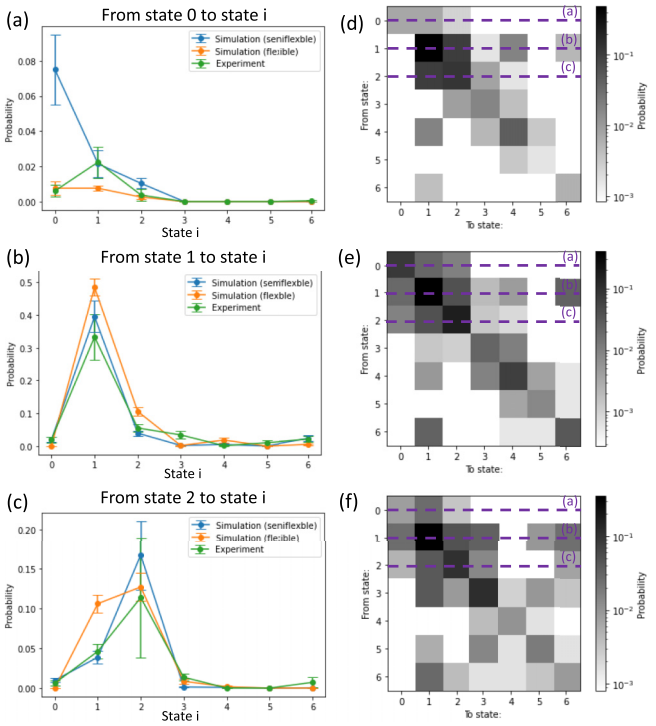

FIG. 15. (a) Transition probability from state 0 to any state. (b) Transition probability from state 1 to any state. (c) Transition probability from state 2 to any state. (d) Transition matrix for simulated flexible chains. (e) Transition matrix for simulated semiflexible chains ($P = 2.5 < D = 6$). (f) Transition matrix for experiments.

One question is the degree of self-entanglement or knotting present versus entanglements or knots formed between the two chains, and how the number of entanglements or knots varies as a function of holding time in the compressed state. Another question is how entanglements or knots will influence chain relaxation and demixing upon zeroing the compressive force.

The present study is entirely based on simulation and experiment, but for a future study the free energy barrier for mixing nucleation could potentially be computed directly as a function of flow speed and chain stiffness and compared to the frequency of nucleation events. For semiflexible chains in particular, mixing might reduce the bending energy by halving the number of bends in each chain. To understand why, assume that the total packing length of both chains combined remains constant whether the chains are mixed or in a demixed state. Geometrically, each chain occupies the whole packing length when mixed, but only half the packing length if demixed, so that the extension of each chain when mixed is necessarily double that when demixed. However, this bending energy economy is achieved only by overcoming the entropic free energy barrier imposed by mixing nucleation. Probing experimentally the mixing dynamics of high stiffness chains would also be an interesting next step; this could be attempted potentially using DNA nanotube constructs produced via DNA nanotechnology [21,22].

ACKNOWLEDGMENTS

This work is supported by the Fonds de recherche du Québec - Nature et technologies (FRQNT) Doctoral Research Scholarship (Award No. 273210), and by the Natural Sciences and Engineering Research Council of Canada (NSERC) Discovery Grants Program (Grant No. RGPIN-2018-06125).

[1] P. G. de Gennes, *Scaling Concepts in Polymer Physics* (Cornell University Press, Ithaca, NY, 1979).
[2] W. Reisner, J. N. Pedersen, and R. H. Austin, DNA Confinement in Nanochannels: Physics and biological applications, Rep. Prog. Phys. **75**, 106601 (2012).
[3] S. Jun and A. Wright, Entropy as the driver of chromosome segregation, Nat. Rev. Microbiol. **8**, 600 (2010).
[4] A. Khorshid, P. Zimny, D. Tétreault-La Roche, G. Massarelli, T. Sakaue, and W. Reisner, Dynamic compression of single nanochannel confined DNA via a nanodozer assay, Phys. Rev. Lett. **113**, 268104 (2014).
[5] A. Khorshid, S. Amin, Y. Zhang, T. Sakaue, and W. Reisner, Non-equilibrium dynamics of nanochannel confined DNA, Macromolecules **49**, 1933 (2016).
[6] S. Bernier, A. Huang, W. W. Reisner, and A. Bhattacharya, Evolution of nested folding states in compression of a strongly confined semiflexible chain, Macromolecules **51**, 4012 (2018).
[7] L. Zeng and W. Reisner, Mixing and demixing arising from compression of two semiflexible polymer chains in nanochannels, Eur. Phys. J. E **46**, 88 (2023).
[8] A. Khorshid, Nonequilibrium physics of nanochannel confned DNA, Ph.D. thesis, McGill University, 2017 (unpublished).
[9] F. Weik, R. Weeber, K. Szuttor, K. Breitsprecher, J. de Graaf, M. Kuron, J. Landsgesell, H. Menke, D. Seana, and C. Holm, Espresso 4.0 - an extensible software package for simulating soft matter systems, Eur. Phys. J.: Spec. Top. **227**, 1789 (2019).
[10] L. Zeng and W. Reisner, Organized states arising from compression of single semiflexible polymer chains in nanochannels, Phys. Rev. E **105**, 064501 (2022).
[11] J. D. Weeks, D. Chandler, and H. C. Andersen, Role of repulsive forces in determining the equilibrium structure of simple liquids, J. Chem. Phys. **54**, 5237 (1971).
[12] T. Soddemann, B. Dünweg, and K. Kremer, A generic computer model for amphiphilic systems, Eur. Phys. J. E **6**, 409 (2001).
[13] L. D. Landau and E. M. Lifshitz, *Statistical Physics* (Pergamon, Oxford, 1969).
[14] S. Amin, A. Khorshid, L. Zeng, P. Zimny, and W. Reisner, A nanofluidic knot factory based on compression of single DNA in nanochannels, Nat. Commun. **9**, 1506 (2018).
[15] A. Huang, W. Reisner, and A. Bhattacharya, Dynamics of DNA squeezed inside a nanochannel via a sliding gasket, Polymers **8**, 352 (2016).
[16] J. B. Bosse, N. S. Tanneti, I. B. Hogue, and L. W. Enquist, Open led illuminator: a simple and inexpensive led illuminator for fast multicolor particle tracking in neurons, PLoS One **10**, e0143547 (2015).
[17] See Supplemental Material at http://link.aps.org/supplemental/10.1103/PhysRevE.109.024501 for a detailed study of the

typical progression of mixing, including examples of such progressions and a detailed analysis of the transition probability matrix.

[18] J. Tang, N. Du, and P. Doyle, Compression and self-entanglement of single DNA molecules under uniform electric field, Proc. Natl. Acad. Sci. USA **108**, 16153 (2011).

[19] D. Michieletto, E. Orlandini, M. S. Turner, and C. Micheletti, Separation of geometrical and topological entanglement in confined polymers driven out of equilibrium, ACS Macro Lett. **9**, 1081 (2020)

[20] J. Rothörl, S. Wettermann, P. Virnau, and A. Bhattacharya, Knot formation of dsDNA pushed inside a nanochannel, Sci. Rep. **12**, 5342 (2022).

[21] D. Schiffels, T. Liedl, and D. K. Fygenson, Nanoscale structure and microscale stiffness of DNA nanotubes, ACS Nano **7**, 6700 (2013).

[22] P. W. K. Rothemund, A. Ekani-Nkodo, N. Papadakis, A. Kumar, D. K. Fygenson, and E. Winfree, Design and characterization of programmable DNA nanotube, J. Am. Chem. Soc. **126**, 16344 (2004).